NANO · MICRO
small
www.small-journal.com

Humidity Assisted Selective Ion Exclusion in 0D Mixed Halide Perovskite Related Structures for Multimode Anti-counterfeiting

*Sumit Kumar Sharma, Monika Salesh, Abinash Tiwari, Sushobhita Chawla, Nitin Pathoor, Sanika S Padelkar, Aftab Alam, Arindam Chowdhury, Balasubramaniam Kavaipatti, and Aswani Yella**

Developing materials that are capable of switching the luminescence in response to a stimuli in solid-state are highly desirable for advanced anticounterfieting applications. Herein, we report 0D mixed halide perovskite-related structures (0D-MHs) that undergo reversible phase transformation in the presence of humidity, which results in the rapid and reversible luminescence color switching from green to red. It is found that selective ion exclusion takes place in the presence of humidity, which results in the formation of either iodide-rich 3D perovskite or bromide-rich 3D perovskite. Iodide-rich 3D perovskite is obtained under high humid conditions with surrounding humidity greater than 60%RH, and bromide-rich 3D perovskite is obtained under low humid conditions with humidity less than 30%RH. This is attributed to the exclusion of MABr owing to its higher solubility in water at room temperature. As long as the reservoir of MAX is present, the decomposition of the 3D- perovskite does not occur, and the reversible transformation and multicolor tunable luminescence is observed. Furthermore, flexible, free-standing films using a composite of PVDF and 0D MH is created which are stable in water and can be used for anti-counterfeiting purposes. The free-standing film remains stable even after a year under ambient room conditions, and the reversible phase transformation still takes place.

1. Introduction

Counterfeiting is a worldwide issue amongst national and financial safeties[1–7] To tackle such issues, anti-counterfeiting applications have been used. Such anti-counterfeiting technologies have developed as a growing application due to their high security codes through information storage and encryption of codes.[5–15] Nowadays, fluorescent materials have served as better anti-counterfeiting material due to their photoemission, which can be easily detected through the human eye.[6,7,9,11,13,15–17] Promising prospects have been shown by smart luminescent materials having multistage emissions due to its high response toward external stimuli when compared to the traditional materials with single emission.[18–25] Such stimuli-responsive smart materials allow us to showcase advanced multi-photoemission modes which are tough to duplicate.

Metal halide Perovskites (MH) are known for their high and intense

---

S. K. Sharma, A. Tiwari, A. Yella
Centre for Research in Nanotechnology and Science
Indian Institute of Technology Bombay
Mumbai 400076, India
E-mail: aswani.yella@iitb.ac.in

M. Salesh, A. Yella
Department of Metallurgical Engineering and Material Science
Indian Institute of Technology Bombay
Mumbai 400076, India

S. Chawla, B. Kavaipatti
Department of Energy Science & Engineering
Indian Institute of Technology Bombay
Mumbai 400076, India

N. Pathoor, A. Chowdhury
Department of Chemistry
Indian Institute of Technology Bombay
Mumbai 400076, India

S. S Padelkar, A. Alam
Department of Physics
Indian Institute of Technology Bombay
Mumbai 400076, India

The ORCID identification number(s) for the author(s) of this article can be found under https://doi.org/10.1002/smll.202412073

DOI: 10.1002/smll.202412073

photo-emission.[26–29] And their emission can be irreversibly tuned by changing their composition.[30–33] It can also be tuned irreversibly by alloying and doping of different metal cations and organic molecules.[34–39] However, this tuned irreversible emission is not desirable as it not possible to develop complicated anti-counterfeiting devices. Although there are some reports of switchable on-off emission and reversible emission in the case of MHs, with the help of external stimuli such as heat, light, water and organic solvents etc[40–43] but they exhibit only single-mode emission.

Halide perovskites can be easily formed due to their low formation energy, but this low formation energy plays a detrimental role in their stability, and can easily decompose in the presence of external stimuli.[44–47] However, this external stimulus-assisted decomposition can help these materials to generate other phases which are difficult to achieve normally.[47–51] This provides an alternate route to tune the properties of these materials. But in most of the cases these transformations are also irreversible in nature. However, low-dimensional perovskites have shown good stability along with promising optoelectronic properties such as high photoemission and reversibly tunable structural and optical properties.[52–61] Dimensionality in MH depends on the degree of connection between BX_6 octahedra. 3D perovskite has cubo-octohedral ABX_3 crystal structure in which BX_6 octahedra are ($B = Pb^{2+}$, Sn^{2+}, $X = I^-$, Br^- and Cl^-) corner shared in all 3D and form an inorganic framework which holds A site cations (methylammonium, formamidinium, Cs^+). While 0D perovskite has A_4BX_6 and $A_4BX_6.2H_2O$ type crystal structure in which BX_6 octahedra are separated by A cation in all 3D.[60] All inorganic Cs_4PbX_6 0D perovskite has been comprehensively studied in past few years.[55,62–64] Response of Cs_4PbX_6 toward different chemical and physical stimuli has also been studied widely and has been reported for anti-counterfeiting applications.[65–68] However, there is not much literature present on methylammonium (MA) and formamidinium (FA) based organic–inorganic hybrid 0D perovskites. Unlike Cs_4PbI_6 0D perovskite, $MA_4PbI_6.2H_2O$ based 0D perovskite hold water molecule to stabilize the crystal in 0D structure. Water molecules in these perovskites are connected to PbX_6 octrahera and MA cation through weak hydrogen bonding, which can easily dissociate by external stimuli such as heat and moisture, and has been reported for switchable solar cells and self-powered humidity sensing applications.[56–58,60,61] Mixing iodide and bromide ions in the perovskite structure typically allows for the band gap tuning, but with the 3D mixed halide perovskites compositional instability is a major issue.[69,70] This compositional instability, called as halide ion segregation, results in the formation of regions with iodide-rich 3D perovskite and some regions with bromide-rich 3D perovskite in the presence of light. So far, not much has been reported with the mixed halide perovskites in the case of lower-dimensional perovskite structures.

Herein, we have studied the effect of humidity on 0—D mixed halide $MA_4PbI_3Br_3.2H_2O$ perovskite related structure, and we have elucidated its reversible transformation from bromine-rich hybrid phase to iodine-rich 3D phase by controlled hydration. This 0D—MH film reversibly switches its color between green, transparent, yellow, red, and brown depending on the surrounding humidity. This humidity-assisted reversible change in its optical appearance is driven through the connection between PbX_6 octahedra, subsequently affecting its dimensionality (**Scheme 1**). Owing to the reversible dimensionality and compositional changes, a tunable multimode emission can be successfully achieved. Finally, we have demonstrated its possible application in multi stage anti-counterfeiting application. This work will provide a valuable insight to develop smart devices which can change their electronic behavior solely by the application of external stimuli.

2. Results and Discussion

In order to explore the mixed halide 0D-MH, thin films of $MA_4PbI_3Br_3.2H_2O$ is fabricated by dissolving MAI, MABr, octyl ammonium bromide, PbI_2 and $PbBr_2$ in 2:2:0.025:0.5:0.5 molar ratio in DMF at room temperature. Then this solution was spin-coated on mesoporous Al_2O_3 coated glass substrate and subsequently heated at 70° C for 20 min. All these processes were done under ambient atmosphere at ≈40% RH. The optical appearance of the film at 60° C is yellow in color (**figure 1a** bottom right). However, just after cooling down to room temperature, the film turned out to be transparent. It is noteworthy that this transparency is maintained between 40 to 50% RH window. Interestingly after reducing the humidity to 30% RH, the film changed to green color, that further gets more dark by reducing the humidity to 10% RH at room temperature. Increasing the humidity to 60% RH, resulted in the transformation from green to transparent to light brown in color. Further increase in the humidity to 90% RH results in darker film. To check if the transformation from green to transparent to dark brown is reversible, we reduced the humidity to 40% RH, and the transformation is found to be completely reversible as the film changed to transparent color. This humidity-assisted reversible color transition is shown in video S1 (Supporting Information).

To gain more insight about this reversible change in color from green to transparent and to dark brown, UV–vis spectroscopy measurements were carried out on the 0D-MH film under different humid conditions. Nitrogen was used as a carrier gas to modulate the humidity during the measurement. Figure 1b,c shows the humidity-dependent absorption spectra and band gap calculated from the absorption edge (from UV–Vis measurements) for 0D-MH thin film. At 40% RH, the absorption spectrum (figure 1b; Figure S1, Supporting Information) reveals a sharp drop in the absorption in the visible region with an absorption edge at 410 nm exhibiting a band gap of 3.03 eV. Upon reducing the humidity to 10% RH, a red shift in the absorption spectrum is observed which also results in band gap reduction to 2.3 eV. As expected from optical appearance, the absorption spectrum at higher humidity (above 60% RH) has drastically red shifted to longer wavelength with absorption edge at 734 nm at 80% RH leading to a band gap of 1.69 eV. The observed absorption edge at 80 %RH is red shifted in comparison to mixed halide 3D perovskite $MAPbI_{1.5}Br_{1.5}$ as shown in the Figure S2 (Supporting Information).

The most exciting feature of this transformation is the complete reversibility of the band gap of this material depending on its surrounding humidity. As the humidity is reduced to 40% RH, the absorption edge shifted back to 410 nm reversibly for many humidity cycles. Each humidity cycle comprises of rising the humidity from 40% RH to 80% RH and reducing it back to 40% RH. Figure 1d shows the wavelength of the absorption

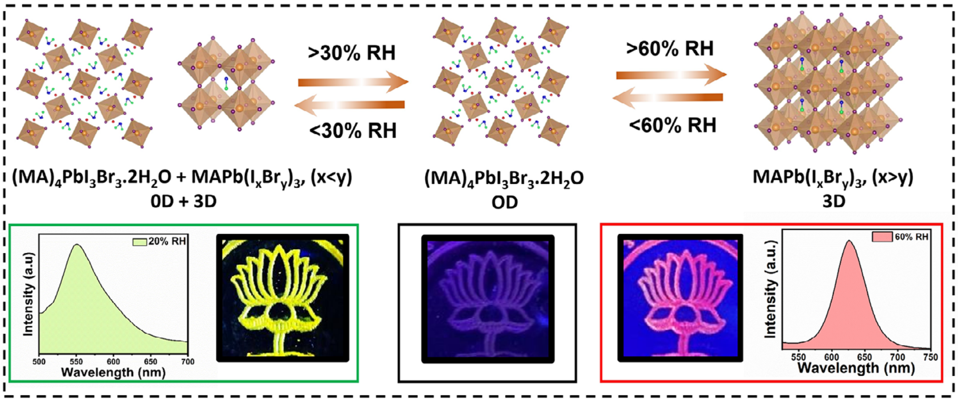

Scheme 1. Reversible transformation from bromine-rich hybrid phase to iodine-rich 3D phase by controlled hydration (top), and the emission can be tuned with the humidity (bottom). The excitation wavelength for all the cases shown in the scheme is 370 nm.

edge over 20 cycles between 40% and 80% RH suggesting an overall smooth, reversible transformation with humidity. Interestingly, when the 0D-MH film is subjected to higher temperature at 60 °C, yellow colored film is observed as can be seen from the optical image in figure 1a (bottom right). UV–Vis absorption spectra is recorded for the 0D-MH film at room temperature and 60 °C and the data obtained is shown in the figure S3 (Supporting Information). From the UV–Vis data, the change in the absorption edge and the corresponding band gap is found to be reversible even with the heat as the stimulus, making the system both as humidochromic and thermochromic material.

To delve deeper into the observed optical change, we carried out the X-ray diffraction (XRD) measurements with varying humidity on the 0-D MH film. **Figure** 2a shows the XRD patterns obtained at different humidity from 10%RH to 50%RH. The film exhibits a 0—D structure at 40%–50% RH window, can be identified by the characteristic reflection at 12.3° corresponding to (011) plane. However, at lower humidity of 20%RH, along with the reflections from the 0D perovskite phase, the reflection at 14.6° gets intensified. These new reflections can be assigned to (001) plane of 3D perovskite ($MAPbX_3$) phase indicating the presence of 3D perovskite within the 0D-MH film. The crystal stability of 0D-MH is also dependent on the presence of two water of

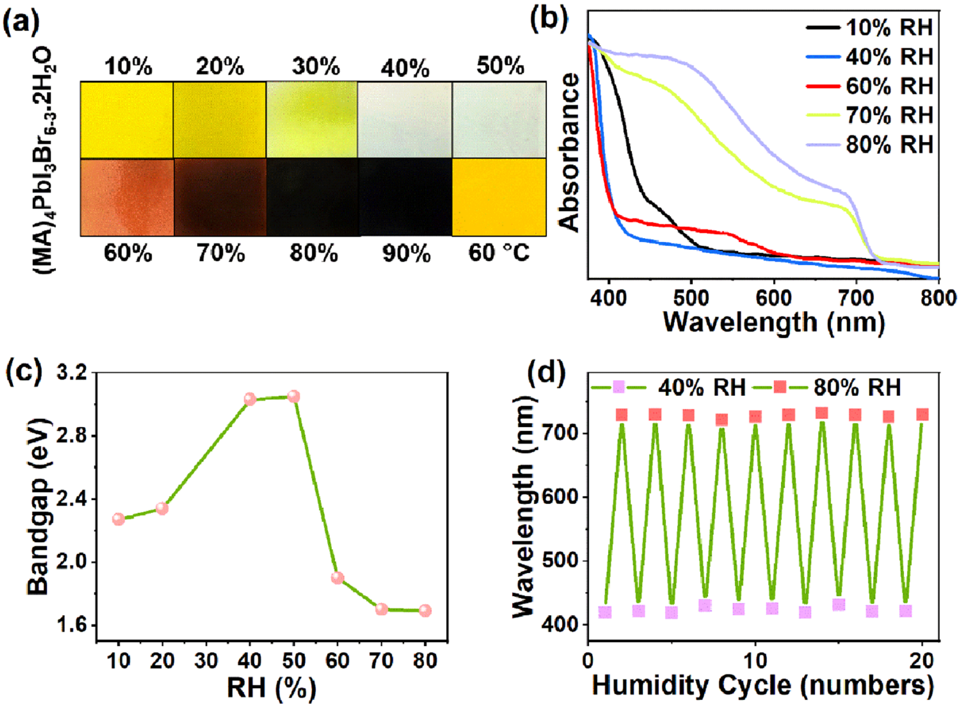

Figure 1. a) Photographs of the 0D-MH films with different appearance depending on the surrounding humidity, b) Humidity-dependent UV–Vis absorption spectrum for 0D-MH film c) Bandgap variation as a function of different humidity d) Reversible change in absorption onset values for 20 cycles between 40% and 80% RH.

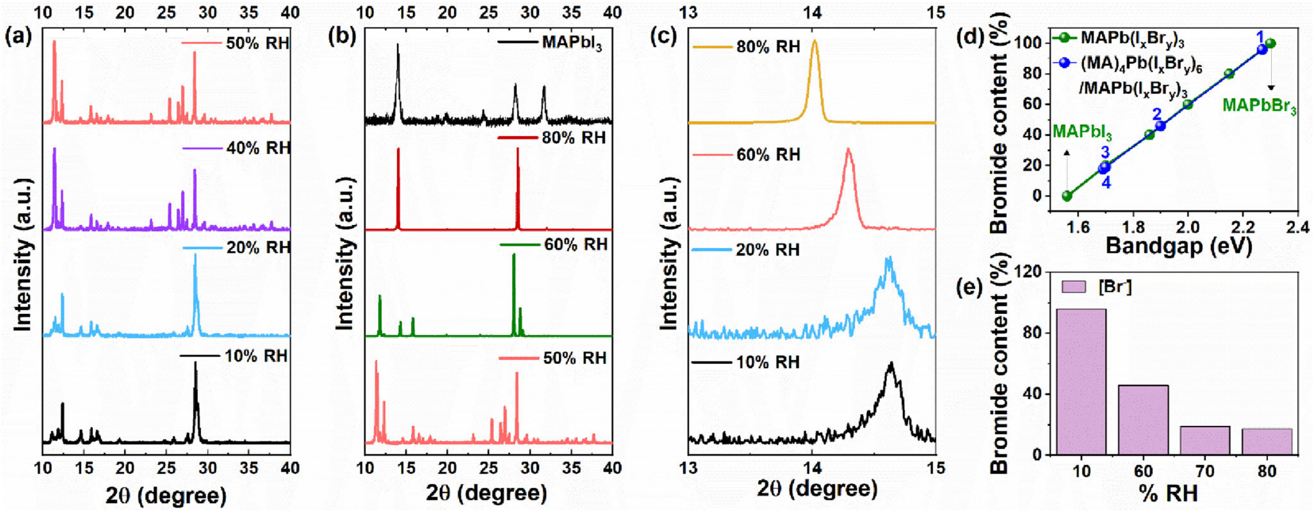

Figure 2. XRD patterns of 0D-MH film at different humidity from a) 10% RH to 50% RH b) and 50% RH to 80% RH b). c) The characteristic peak of (001) plane at different humidities. d) Determination of halide content in converted 3D perovskite phase where point 1,2,3, and 4 represent the phases at 10% RH, 60% RH, 70% RH and 80% RH respectively, e) Represents the different bromide concentration (%) at different humidity window (10%–80% RH). Further confirming the presence of more iodide ion in the converted 3D phase at higher humidity and more bromide ions at lower humidity as depicted in the histogram.

crystallization within the structure. These water molecules are connected to the system through weak H-bond and can be easily broken by reducing humidity in the surrounding atmosphere. Lack of water at lower humidity facilitates the coupling of PbX_6 octahedra within the 0D MH resulting in the formation of 3D perovskite along with 0D MH,[57] which can also be observed through the red shift in the absorption spectrum at lower humidity as seen in the figure 1b.

figure 2b shows the diffraction patterns obtained with increasing humidity from 50%RH to 80%RH. Increasing the humidity to 60%RH resulted in the formation of 3D perovskite indicated by the reflection at 14.3° corresponding to the (001) plane. Further increase above 60%RH resulted in the formation of phase-pure 3D perovskite as shown in the figure 2b. All reflections related to the 0-D perovskite phase completely vanished at 80% RH resulting in the formation of a pure 3-D perovskite. This dimensionality increment at higher humidity is facilitated by the dissolution of the excess MAX presented in the 0D-MH system. Consequently, initially isolated PbX_6 octahedron get rearranged and coupled into 3D network, resulting in the formation of 3D perovskite.[56,57,60] The process is illustrated through the following reaction

$$MA_4PbX_6.2H_2O = MAPbX_3 + 3MAX + 2H_2O\,(\text{where}\; X = I,\; Br) \quad (1)$$

Since the 0D perovskite is a mixed halide (iodide and bromide) perovskite, exclusion of MABr or MAI can take place with the humidity. Now the system can have three different options for the exclusion, which makes it challenging.

To understand whether the MABr or MAI exclusion takes place with different humidity, the reflection corresponding to (001) plane of $MAPbX_3$ obtained at different humidity is compared with the characteristic (001) reflection corresponding to regular 3-D $MAPbBr_3$ and $MAPbI_3$ perovskites (figure S4; figure 2c, Supporting Information). Figure S4 (Supporting Information) shows the XRD pattern of the 0D-MH film at 5%RH and is compared with the standard 3D $MAPbI_3$ and $MAPbBr_3$ patterns. It is clearly visible that the (001) reflection resides at a higher angle when compared to $MAPbI_3$ perovskites and close to the characteristic peak of $MAPbBr_3$ perovskite. This suggests that the formation of 3D perovskite at low humidity is mainly dominated by the corner sharing of $PbBr_6$ octrahedra resulting in the formation of bromide rich 3D perovskite. figure 2c compares the position of the (001) reflection at 10%, 20%, 60% and 80%RH. Interestingly, at 60% RH the (001) reflection is shifted to a lower diffraction angle (14.3° at 60%RH), which further shifted to lower angle (14.1 at 80% RH) upon increasing the humidity to 80% RH (Figure 2c). When compared to the conventional 3D $MAPbI_3$ and $MAPbI_{1.5}Br_{1.5}$ perovskites, the characteristic perovskite peak at 14.1° at 80% RH resides close to the $MAPbI_3$ phase as shown in the Figure S5 (Supporting Information), indicating the presence of more iodide ions in the crystallized 3D perovskite.

As the optical properties and band gap of perovskites is highly dependent on the type of halide present in the system. Hence, the actual estimation of halide concentration present in the converted 3D part at different humidity is essential. Halide concentration can be obtained through the band gap energy of perovskite due to its linear correlation with the halide present in the system.[42,71] We have established a regression equation ($Y = 0.0074*X + 1.560$) by considering the bromide content of $MAPbI_3$ as 0% with a band gap of 1.55 eV and as 100% in case of $MAPbBr_3$ with a band gap of 2.3 eV. Subsequently, the band gap value of 0D-MH at different humidity were used to obtain the halide composition of the converted 3D phase by using the same regression equation. For instance, the bromide content in converted 3D phase at 80% RH turn out to be ≈18% and can be expressed as $MAPb(I_{0.82}Br_{0.18})_3$, further confirming superior doping of iodide ions in converted 3D phase in water-rich conditions (figure 2d). While in the case of lower humidity (10% RH), elevated concentration of bromide ion of roughly 96% confirms the presence of more bromide ions in the partially converted 3D phase which can be expressed as $MAPb(I_{0.04}Br_{0.96})_3$. Here the phases at 40% and 50% RH has been excluded for this calculation as material exists in pure 0D phase at these humidity as confirmed by XRD. Furthermore, for better understanding the calculated ionic concentration of 3D phase has been presented by histogram (figure 2e) against the surrounding humidity, indicating the humidity-dependent selective ion migration of iodide and bromide ions. Moreover, to validate the calculated halide ratios at higher humidity for $MAPb(I_{0.82}Br_{0.18})_3$ phase, $MAPb(I_{0.82}Br_{0.18})_3$ 3D MH were synthesized by maintaining the stoichiometric ratio of I/Br to 82%/18%. Then the absorption spectra of this thin film was compared with the forementioned phase at 80% RH (Figure S6, Supporting Information). A very slight difference in the absorption edge was observed which further confirms the formation of $MAPb(I_{0.82}Br_{0.18})_3$ perovskite at higher humidity. We also carried out the XRD studies on 0D-MH films with the temperature as the stimulus, and figure S7 (Supporting Information) shows the patterns obtained at 25 °C, 60 °C and after cooling back to 25 °C. It is clear that at 60 °C, the 0D-MHs convert to a mixed 0D and 3D perovskite system, with the 3D perovskite being rich in Bromide content, similar to the low humid conditions. This transformation can be represented in the following way.

$$aMA_4Pbl_3Br_3 + (1 - a)\,MAPb\left(l_XBr_Y\right)_3, x << y$$

$$\xleftarrow{<40\%\ RH} MA_4PBl_3Br_3 \xrightarrow{(>60\%\ RH)} MAPB\left(l_XBr_Y\right)_3, x << y \qquad (2)$$

Excess MABr and MAI present in the system excludes out of the 0D MH system, depending on the surrounding humidity subsequently facilitating the formation of 3D MH ($(MAPb(I_XBr_{1\text{-}X})_3$). The formation of the iodide-rich and bromide-rich 3D perovskites are high and low humidity could be due to the difference in the solubility of MABr and MAI. MABr has comparatively higher water solubility than MAI which leads to more dissolution of MABr, leaving excess MAI at higher humidity to take part in 3D MH formation, resulting in the formation of iodide-rich 3D perovskite. In order to support this plausible explanation, we have fabricated the thin films of pure iodide-based MA_4PbI_6 and bromide based MA_4PbBr_6 perovskite. Subsequently XRD was performed on these films to understand their humidity assisted 0D to 3D conversion. As shown in the figure S8 (Supporting Information), this humidity-assisted 0D to 3D transformation take place at 60% RH in case of MA_4PbBr_6 perovskite while in case of MA_4PbI_6 perovskite, this transformation happened at 70% RH clearly indicating the shift in transition humidity point. This mismatch in transition humidity point could be associated with the different solubility of MABr and MAI salt in water. This means that MABr can easily absorb the water at lower humidity and comes out of the system. Similarly, in case of 0D-MH, dissolution of MABr takes place at 60% RH leaving more iodide ions in the system for the formation of iodide-rich 3D perovskite at higher humidity.

To understand the phase purity of 0D MHs as a function of relative humidity, Rietveld refinements were carried out on the XRD patterns. The crystal structures of $MA_4PbI_6.2H_2O$ and $MA_4PbBr_6.2H_2O$ have been reported previously.[57] Based on this, we varied the occupancy and Pb—Br/Pb—I bond lengths to find suitable lattice parameters and bond lengths for a single 0D-$MA_4PbI_3Br_3$ phase. However, we found that between 40–50%RH in the case of the mixed halide 0D MH, halide segregation takes place and splits equally into 0D $MA_4PbBr_6.2H_2O$ and 0D $MA_4PbI_6.2H_2O$. We also observe some texturing or preferential orientation in these films. Figure S9 (Supporting Information) provides a refinement of the films prepared at different relative humidity. The unrefined less intense peaks (in the range of 16° – 17°) probably belong to 0D perovskite phase, as these reflections are not present in the 80%RH case. If these reflections arise from any decomposition products like Pb(OH)X, then these should be dominant at 80%RH when the MAX is solvated in the presence of humidity, which is not the case. Hence, these reflections could be attributed to the mixed halide $MA_4PbI_3Br_3.2H_2O$ phase which cannot be refined in the absence of a pure PXRD or SCXRD. Figure S10 (Supporting Information) shows the simulated pattern for the mixed halide $MA_4PbI_3Br_3.2H_2O$ using the crystalmaker software. The calculated ratio of the weight percentages for the observed two phases is $MA_4PbI_6.2H_2O$:$MA_4PbBr_6.2H_2O$ is ~1:1. For other humidity conditions the phase fraction of the 0D and 3D structures obtained after refinement has been summarized in the **Table 1** given below. Table S1 (Supporting Information) of the supporting information shows the crystallographic parameters estimated from the Rietveld refinement of the 0D-MH samples with different humidity conditions, along with phase quantification.

Humidity treatment does not show any adverse effect on the local chemical environment and morphology of the film as confirmed by the XPS and SEM analysis. Figure S11 (Supporting Information) shows the XPS spectra of as prepared and humidity-treated (20 cycles) 0D-MH films. No change has been observed in binding energy for all elements even after several cycles of humidity treatment. To know the effect of the moisture treatment on the morphology of the film, we have carried out the scanning electron microscopy imaging on the 0-D perovskite film with and without humidity treatment. Figure S12a,b (Supporting Information) shows the SEM images of as prepared $MA_4PbI_3Br_3$ perovskite film and after treating the same film with 80% RH, respectively. A slight improvement in the surface coverage after humidity treatment is observed from SEM images.

In order to further decipher the 0D MHs optical properties, steady state photoluminescence (PL) spectra under different humid environment were carried out (**figure 3a**; Figure S13, Supporting Information). At 40% RH, 0-D perovskite shows a weak emission centered at 540 nm, and this emission is highly Stokes-shifted compared to UV absorption edge at 40% RH. An increase in humidity to 60% RH leads to a red shift in the spectra with a standard Gaussian peak centered at 630 nm, which gets further red-shifted to 740 nm at 80% RH. However, emission intensity at higher humidity (80% RH) is less in comparison to emission at 60%RH. The red shift in the emission observed at 60% and 80% RH can be attributed to the formation of the iodide-rich 3D perovskite as the humidity is increased from 40% to 60% and then to 80% humidity. At high humid conditions, complete phase change from 0D MHs to 3D perovskite is observed, and we attribute the increase in the PL from 40% to 60% to the increase in the fraction of 3D perovskite in the film. At 40% RH, from XRD measurements, only 0D phase is present whereas at 60% RH, 48% of 0D is converted to 3D perovskite phase. Reduction in the humidity to 20% RH and below resulted in PL at 550 nm with increased PL

Table 1. Phase fraction of the 0D MHs and 3D perovskite obtained from the Rietveld refinement of the XRD patterns at different humidity.

	0D	0D	3D	3D
% RH	$MA_4PbBr_6.2H_2O$ (%)	$MA_4PbI_6.2H_2O$ (%)	$MAPbBr_3$ (%)	$MAPbI_3$ (%)
80	–	–	–	100
60	52.1	–	–	47.9
40	58	42	–	–
10	32	61	7	–

intensity compared to 40%RH. Also the PL observed at 10%RH is very broad, ranging from 500 to 650 nm. The broad emission could be attributed to two factors, the presence of self-trapped excitons (STEs) arising from the octahedral distortions or due to the presence of mixed halides with differing halide compositions.

To see if the broad emission observed at low humid conditions is due to the self-trapped excitons (STEs) arising from the octahedral distortions, we also carried out ab-initio density functional theory calculations on $MA_4PbI_3Br_3$ structure with various coverage of relative humidity (RH) viz., 20% RH, 40% RH 60% RH, and 80% RH. Figure S14 (Supporting Information) shows the optimized structures at different humidity. Based on the simulated intra-octahedral distortion factors (Table S2), 0D $MA_4PbI_3Br_3$ with 20% RH and 60% RH have a potential likelihood of exhibiting wider FWHMs and hence presence of STEs, we calculated the imaginary part of the dielectric function to capture the exciton states, including both singlet and triplet excitonic states. Figure S15 (Supporting Information) depicts the imaginary part of the dielectric function simulated for $MA_4PbI_3Br_3$ (20% RH), $MA_4PbI_3Br_3$ (40% RH), and $MA_4PbI_3Br_3$ (60% RH) optimized structures. However, no STE emission states were detected for any of these cases despite of strong octahedral distortion.

From the experiments, the emission mainly arises from the 3D structure, as no significant emission is observed at 40% RH where only 0D-MH phase exists. Figure S16 (Supporting Information) shows the Gaussian fitting of the PL spectra obtained at 10% and 60% RH. It can be seen that the PL spectra can be fitted using two Gaussians centred at 550 nm and 605 nm, with the 550 nm one being more intense. The FWHM of the corresponding peaks centered at 550 nm and 605 nm is 44 and 72 nm, respectively. From the XRD refinement, 3D phase in the low humidity case corresponds to $MAPbBr_3$ occurring in the space group, $Pm\bar{3}m$ with perfect octahedral symmetry and has no octahedral distortion. Hence, the broad emission seen at low humidity could not be attributed to STEs arising from the distortion in the octahedra. So, we attribute the intense emission centered at 550 nm with an FWHM of 44 nm to that of the cubic $MAPbBr_3$ perovskite, and the emission centered at 605 nm with an FWHM of 72 nm is attributed to the formation of mixed halide 3D perovskite, albeit in quantity undetectable by XRD. The FWHM of the high humid phase has a single gaussian PL

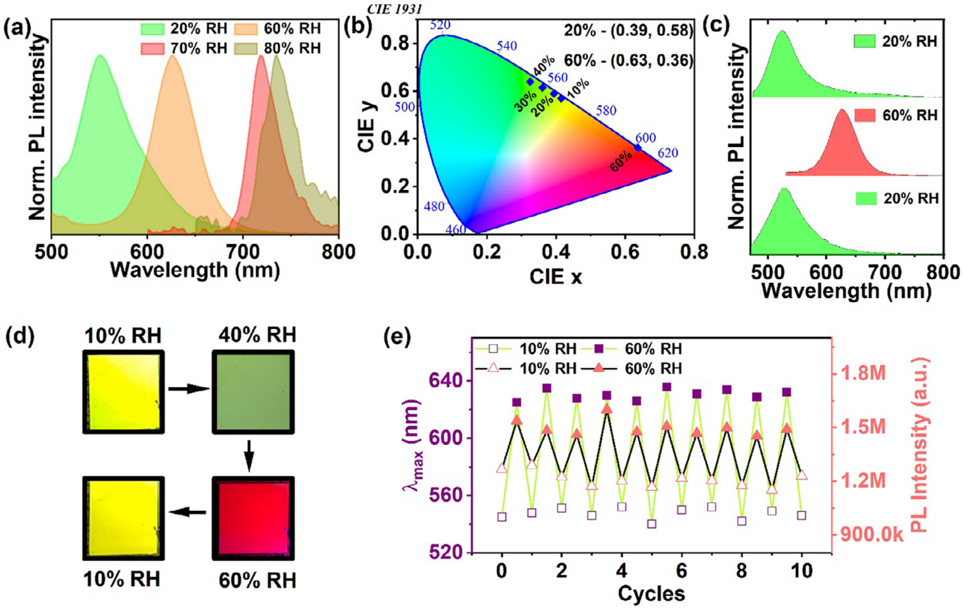

Figure 3. a) Normalized PL spectra of 0D-MH at different humidity levels, suggesting drastic red shift in emission wavelength. b) Initial green emission at lower humidity RH tuned to red emission at 60% RH as confirmed by the CIE plot. c) This tuned red emission at 60% RH again blue shifted to green emission by reducing the surrounding humidity to 20% RH as confirmed by the PL spectra.d) optical images of 0D MH thin film showing intense emission under 370 nm UV light at different humidity. Initial yellowish green emission at lower humidity reversibly changed to green at 30% RH and red emission at 60% RH. e) reversibility of PL emission between 10% RH and 60% RH for 10 cycles and stable PL intensity at corresponding humidity.

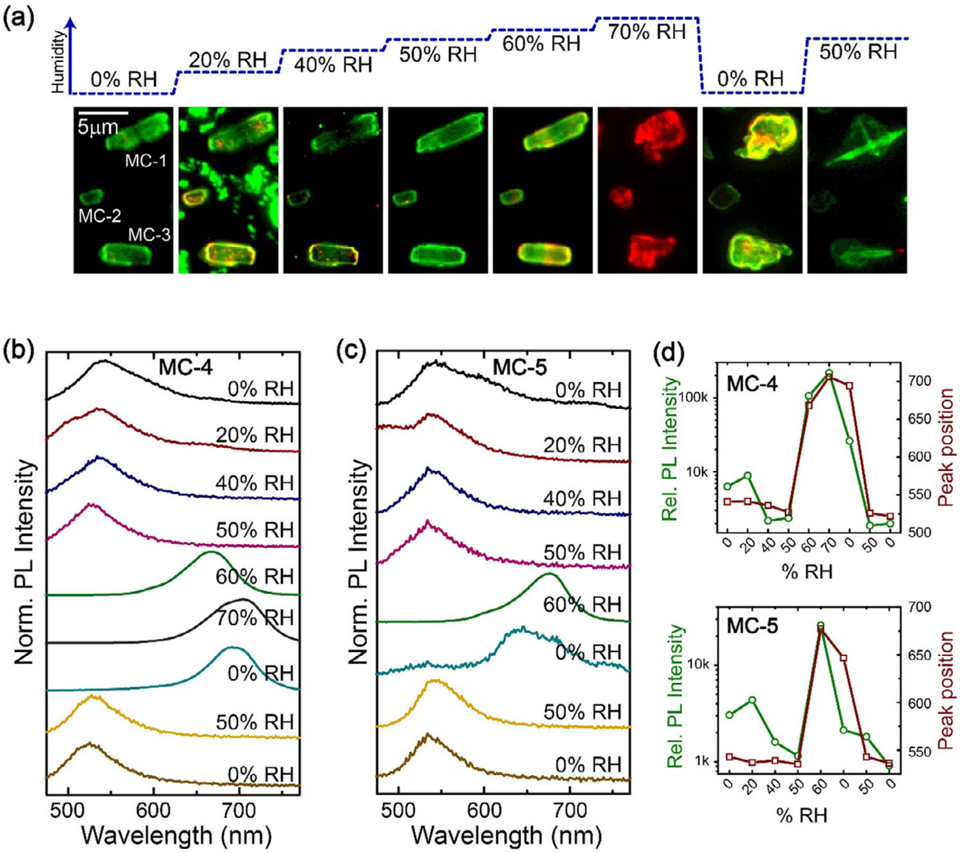

Figure 4. a) Pseudo true color PL images of microcrystals of 0D-MH at different humidity b,c) Humidity-dependent PL spectra of two representative individual crystals. d) PL intensity and peak position as a function of the RH for MC-4 and MC5.

centered at 630 nm with a FWHM of 53 nm at 60% RH. This is comparable to the tetragonal $MAPbI_3$ phase reported in the literature, even though the high humidity 3D phase crystallized in the orthorhombic space group, Fmmm (a phase with distorted octahedra). To further confirm that the broad emission is not a result of STEs, we carried out the photoluminescence lifetime measurements at 10%, 60% and 80% RH, and the average PL lifetime values are 2, 13, and 0.4 ns, respectively (Figure S17, Supporting Information). These lifetime values are very short in comparison to typical STE emissions.

This shift in green to red emission under different humidity can be distinctly visible and can be seen through figure 3b–d. CIE color space plot is shown in the figure 3b to highlight the better color variation representation of the emissions for mixed halide perovskite at different ranges of humidity. The color space coordinates at 20%RH were (0.39, 0.58), showing green emission, and with the higher humidity, the coordinates shifted to (0.63, 0.36), indicating red emission. Complete reversible fluorescence shift from red to green is noticed under decreasing the humidity level from 80%RH to 40%RH. Figure 3c shows the shift in the PL spectra observed during one humidity cycle. These swift changes in emission can be visually seen under 370 nm of UV light as shown in Figure 3d. Even after 10 complete cycles of hydration and dehydration, there is not much change observed in the emission peak wavelength and intensity as shown in the Figure 3e, which suggests a remarkable emission tunability and stability. To the best of our knowledge, this kind of reversibility in colors from green to red emission in A_4PbX_6 perovskite has not been reported previously.

To gain more insight into this observed humidity-driven reversible green to red emission, and check whether such behaviors are uniformly observed for all the crystals, we performed spectrally resolved PL microscopy on individual crystals. A series of PL images of the same crystals were collected via two detection channels at various ambient humidity (RH) to visualize the color of emission as a function of RH, as presented in **Figure 4**a. These pseudocolor PL images show spatially segregated crystals whose emission color is green at low RH. As the ambient humidity increases (till 40%), we observed a slight blue shift, the rate of which can vary slightly over different crystals. The color, however, stabilizes back to green when the RH reaches ~50%. Upon an increase in the moisture in the local atmosphere, we observed a red shift beyond 50% RH, the rate of which further shoots up while moving from 60% to 70% RH. It is noted that the emissivity of the MCs reduce significantly when the RH is increased beyond 70%. Interestingly, this rapid spectral shift with humidity is accompanied with a change in the shape of these crystals, which was observed previously for the pure bromide counterpart of this material.[55] Further, these color changes are found to be reversible -the decrease in RH showed blue-shift in emission wavelength, and the process of reversal from red to green emission was stabilized at 50% RH, which was found to be reversible

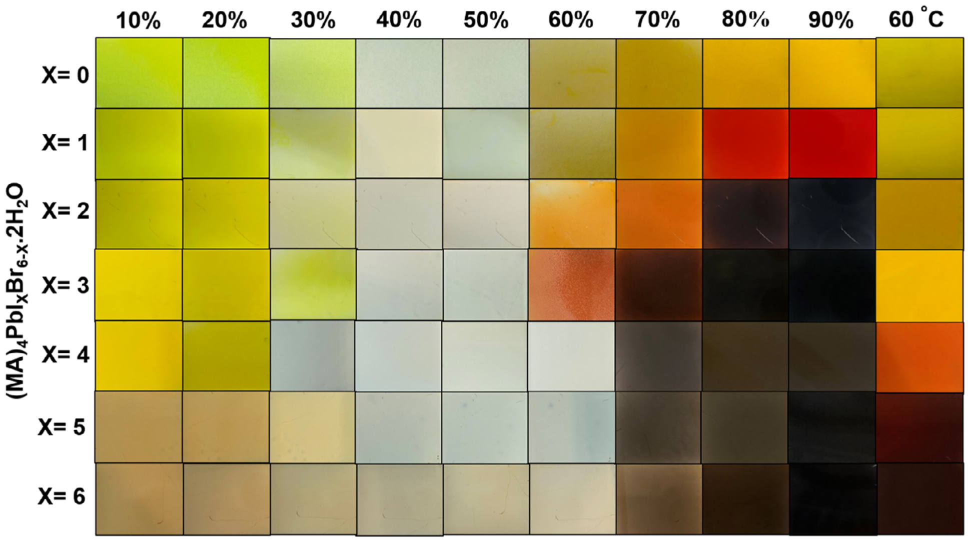

Figure 5. a) Optical images of $MA_4PbI_XBr_{6\text{-}X}.2H_2O$ perovskite films over varying humidity collected at different halide compositions (I/Br ratio).

over multiple cycles (Figure S18, Supporting Information). It should be noted that, while decreasing the RH, assessing the level of moisture adsorbed on (or interact with) the crystals becomes challenging. We purged dry nitrogen over half an hour before the recovery of yellowish-green emission from these crystals. The average PL spectra from two different crystals are shown in Figure 4b,c, which provides an accurate spectral response of the emission of these crystals based on the humidity of the atmosphere. The relative PL intensities and peak positions of MC-4 and MC-5 (Figure 4d) reversibly change in spectral position as mentioned earlier, and the associated emission intensity maximize between 560–70% RH. The formation of iodide-rich nanodomains can result in an effective migration of charge carriers into this smaller band-gap domains can explain the collective spectral shift. There exists a behavioral heterogeneity among the two representative crystals, in terms of the rate of color change, however, the general trend mentioned above is found to be consistent in all the studied samples.

A wide range of color tunability in response to humidity and heat can also be achieved by changing the ratio of halide within a film. **Figure 5** shows the optical images from the respective perovskite films coated on alumina to get a wide range of color through varying the I/Br ratio. The XRD for all the respective films at 40%RH are shown in Figure S19 (Supporting Information). The shift in characteristic peak of 0D perovskite between 11° – 12° 2θ value to higher values with an increase in bromine concentration portrays an effective participation of Br^- ion in 0D perovskite phase formation. Based on these optical affirmations, the single source material shows a dynamic multicolor window ranging from 10%-90% RH and also for 60 °C, covering a wide range of color gamut that can be detected visually for advanced anti-counterfeiting devices. Additionally, the emission from these materials can also be modified or tuned with different RH windows as well as different I/Br ratios. Moreover, these different color emission patterns from a single material can provide a building block for multistage anti-counterfeiting and security applications.

Inspired through all the dynamic emission from this single component, this material has the potential for multistage anti-counterfeiting or ultrahigh-sensitivity applications of specific wavelength. So, to see the 0D MHs potential in multicolor luminescence anti-counterfeiting, we designed the flower pattern created by laser engraving an acrylic sheet and spin coating the 0D-MH perovskite solution on top of it followed by annealing at 70 °C. These carved structure presents multi-level of security under different conditions. **Figure 6a** (top row) shows the samples placed under visible light at different %RH particularly, 10% RH, 30%RH, 45% RH and 65% RH which showed a gradation of yellow to transparent to light red under visible light. Now under the realm of excitation with 370 nm, the codes appear to be yellow, green and bright red respectively (figure 6a bottom row). It is also noteworthy that amongst two successive emissions, there can be intermediate emissions in between these phases. All these emissions are visually detected rather than usage of any radiation detection sensors or any such security instrument. The reversibility of the encryption and decryption process is also a critical parameter for information security applications. To evaluate this, 20 cycles of varying humidity was carried out for the 0D MH films, and as shown in the Figure S20 (supporting information), PL intensity is maintained as the initial value even after 20 consecutive switching cycles. Also, the FWHM of the film for the flower pattern remains nearly unchanged even after 20 humidity cycles. So, this shows that the 0D MHs can be effectively applied for the information encryption and decryption.

To further increase the complexity of security in a system against counterfeiting, we developed a cherry pattern whose leaves constitute MA_4PbBr_6 while its fruit constitutes to that of $MA_4PbI_3Br_3$ 0D MH. These patterns shown in Figure 6b, also presents a localized dual emission representing MA_4PbBr_6, having green emission at lower humidity and the other part having a greenish yellow emission, while the fruit shows red emission on exposure to high humidity of 60 RH% under UV light. But apart from PL quenching there is no emission transformation noticed

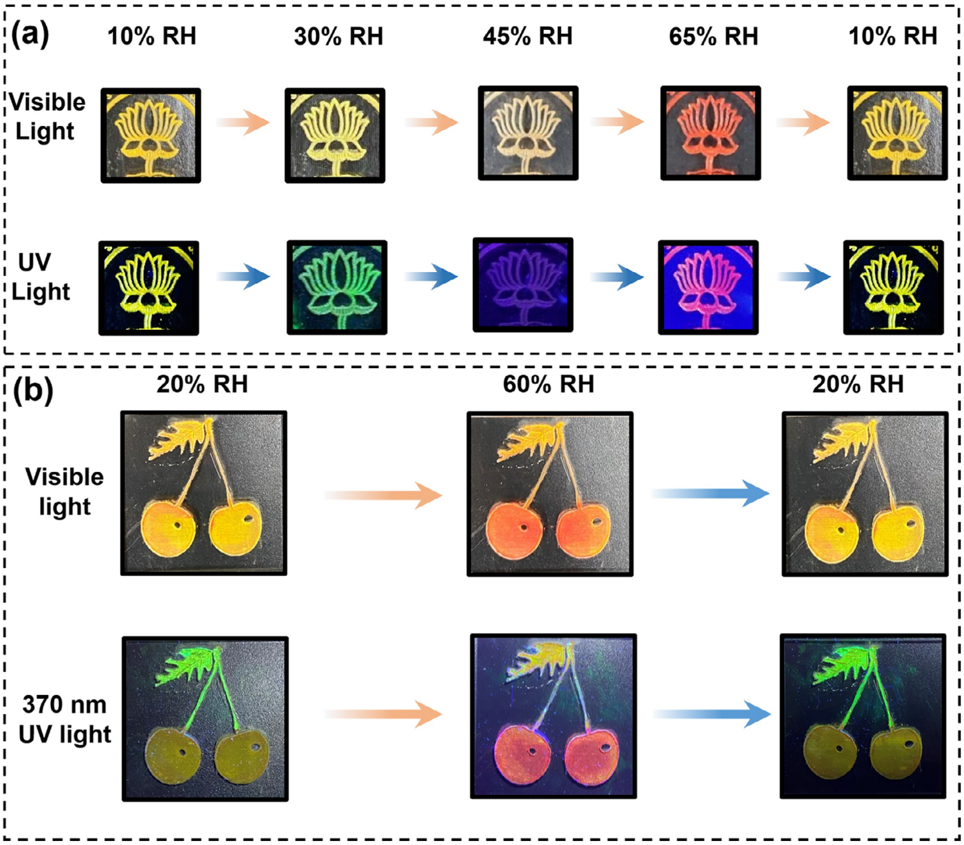

Figure 6. a) (top row) 0D-MH coated flower pattern at different humidity in visible light and (bottom row) respective optical images in 370 nm UV light showing multimode emission. b) (top row) showing the cherry pattern at different humidity, where stems were made using 0D MA_4PbBr_6 perovskite and fruit was created by using 0D-MH, and (bottom row) respective images in 370 nm UV light.

for the leaves having MA_4PbBr_6 as there is no iodide ions present in the system to tune the emission.

Developing and maintaining the multimode emission of a perovskite composite free-standing film in a polymer matrix remains challenging for flexible anti-counterfeiting applications. The limitations are caused due to the hindrance of external stimuli when incorporated with polymers. Thus, to further elucidate such flexible multimode anti-counterfeiting applications in a wider field, we have fabricated a flexible 0D-MH and PVDF composite film in a weight ratio of 1:20. These fabricated free-standing films appeared yellow in color when treated under 40% RH humidity (**figure** 7 top row) and exhibited a bright green emission under 370 nm excitation (figure 7 bottom row). Additionally, a localized high humidity was provided to an area of 0.5 cm in diameter through a pipe carrying water vapor. The as treated area appears to give a localized red emission while the other part of the film appears having green emission, depicting a lower humidity phase. Further to check the effect of higher humidity on a larger scale area, the entire film was submerged in water for 10 s. Video S2 (Supporting Information) shows the film under UV light. A strong red emission appeared throughout the film, even after completely merging in the water. And when the film was taken out of water, the portrayed red emission gradually switches back to the original green emissive state. To check the long-term stability of this 0D MH and polymer composite in harsh conditions, we soaked the film for 10 min in water. And it showed a stable red emission as can be seen in Figure S21 (Supporting Information). Upon taking it out of water, it switched back to a green emissive state. Later the same film was stored under ambient conditions for ≈6 months, and found that the switchable green to red emissive state was still intact, portraying its long-term stability (Figure S22, Supporting Information). Video S3 (Supporting Information) shows the cyclability of the thin film 0D MHP coated on the glass.

3. Conclusion

In conclusion, we have shown that 0D MHs undergo humidity-mediated selective ion exclusion which results in the formation of either iodide-rich 3D perovskite or bromide-rich 3D perovskite. Iodide-rich 3D perovskite is obtained under high humid conditions with surrounding humidity greater than 60%RH. Bromide rich 3D perovskite is obtained under low humid conditions with humidity less than 30%RH. This is attributed to the exclusion of MABr owing to its higher solubility in water at room temperature. This selective exclusion of MABr at high humid conditions resulted in the red shifted absorption and a corresponding decrease in the band gap. Under low humid conditions also, red shifted absorption is observed which resulted in the transformation from 0D perovskite to bromide rich 3D perovskite. Owing

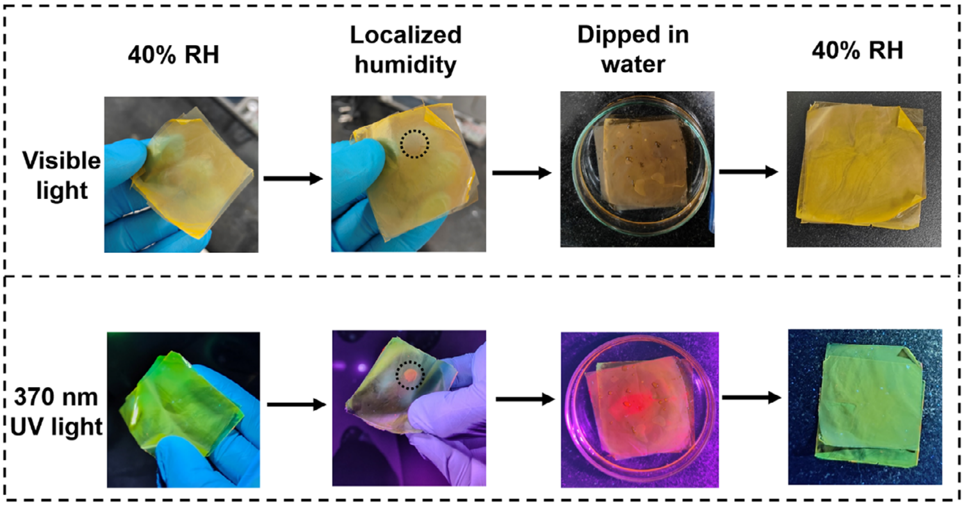

Figure 7. (top row) Flexible 0D-MH and PVDF composite free-standing film in visible light and **(bottom row)** and under 370 nm UV light.

to the change in the band gap, multicolor tunable luminescence was observed at different humid conditions which is reversible as well. We have further shown that this humidity-mediated fluorescence from a single component material offers a simple, practical yet compatible multistage anti-counterfeiting for information security applications. A robust composite of PVDF and 0D MH was also developed as flexible free-standing films for anti-counterfeiting applications based on the 0D MH emissive hydrochromic smart materials.

Supporting Information

Supporting Information is available from the Wiley Online Library or from the author.

Acknowledgements

This work is primarily supported by the Science and Engineering Research Board, Government of India, under Grant Number SPG/2021/004745-G. A.T. thanks the Council for Scientific and Industrial Research (CSIR), India, for the fellowship. The authors acknowledge Mr. Suraj Singh for help with the humidity-dependent XRD.

Conflict of Interest

The authors declare no conflict of interest.

Data Availability Statement

The data that support the findings of this study are available from the corresponding author upon reasonable request.

Keywords

anti-counterfeiting, dimensionality, halide perovskites, luminescence, polymer composites

Received: December 12, 2024
Revised: July 14, 2025
Published online: August 1, 2025

[1] K. P. Pfeuffer, J. Caldwell, J. T. Shelley, S. J. Ray, G. M. Hieftje, *Analyst* **2014**, *139*, 4505.
[2] G. Gistri, S. Romani, S. Pace, V. Gabrielli, S. Grappi, J. Brand Manag, **2009**, *16*, 364.
[3] E. L. Prime, D. H. Solomon, *Angew. Chem., Int. Ed.* **2010**, *49*, 3726.
[4] M. A. Moon, B. Javaid, M. Kiran, H. M. Awan, A. Farooq, *Marketing Intelligence & Planning* **2018**, *36*, 794.
[5] R. Li, Y. Zhang, J. Tan, J. Wan, J. Guo, C. Wang, *ACS Appl. Mater. Interfaces* **2016**, *8*, 9384.
[6] W. Ren, G. Lin, C. Clarke, J. Zhou, D. Jin, *Adv. Mater.* **2020**, *32*, 1901430.
[7] A. Abdollahi, H. Roghani-Mamaqani, B. Razavi, M. Salami-Kalajahi, *ACS Nano* **2020**, *14*, 14417.
[8] Y. Sun, X. Le, S. Zhou, T. Chen, *Adv. Mater.* **2022**, *34*, 2201262.
[9] T. Zhang, L. Wang, J. Wang, Z. Wang, M. Gupta, X. Guo, Y. Zhu, Y. C. Yiu, T. K. C. Hui, Y. Zhou, C. Li, D. Lei, K. H. Li, X. Wang, Q. Wang, L. Shao, Z. Chu, *Nature Commun* **2023**, *14*, 2507.
[10] H. Zhang, X. Ji, *ACS Cent. Sci.* **2022**, *8*, 507.
[11] X. Yu, H. Zhang, J. Yu, *Aggregate* **2021**, *2*, 20.
[12] Y. Heo, H. Kang, J. S. Lee, Y. K. Oh, S. H. Kim, *Small* **2016**, *12*, 3819.
[13] J. W. Leem, H. J. Jeon, Y. Ji, S. M. Park, Y. Kwak, J. Park, K. Y. Kim, S. W. Kim, Y. L. Kim, *ACS Cent. Sci.* **2022**, *8*, 513.
[14] J. C. Guirado-Moreno, M. Guembe-García, J. M. García, R. Aguado, A. J. M. Valente, S. Vallejos, *ACS Appl. Mater. Interfaces* **2021**, *13*, 60454.
[15] J. Zhang, Y. Liu, C. Njel, S. Ronneberger, N. V. Tarakina, F. F. Loeffler, *Nature Nanotechnol* **2023**, *18*, 1027.
[16] A. Abdollahi, K. Sahandi-Zangabad, H. Roghani-Mamaqani, *ACS Appl. Mater. Interfaces* **2018**, *10*, 39279.
[17] F. Li, X. Wang, Z. Xia, C. Pan, Q. Liu, *Adv. Funct. Mater.* **2017**, *27*, 1700051.
[18] A. Abdollahi, B. Ghasemi, S. Nikzaban, N. Sardari, S. Jorjeisi, A. Dashti, *ACS Applied Materials Interfaces* **2023**, *15*, 7466.
[19] M. Cai, T. Lang, S. Fang, T. Han, D. Valiev, H. You, C. Liu, J. Yu, P. Su, X. Jing, G. Ge, B. Liu, E. F. Polisadova, *J. Lumin.* **2023**, *257*, 119713.
[20] P. Pei, R. Wei, B. Wang, J. Su, Z. Zhang, W. Liu, *Adv. Funct. Mater.* **2021**, *31*, 2102479.
[21] B. Xiao, P. Xiong, S. Wu, D. Jiang, K. Chen, Y. Xiao, P. Shao, Y. Wang, *Adv. Opt. Mater.* **2023**, *11*, 2300911.
[22] Y. Luo, L. Zhang, Y. Liu, E. Heydari, L. Chen, G. Bai, *J. Am. Ceram. Soc.* **2022**, *105*, 1375.

[23] D. Gao, Q. Kuang, F. Gao, H. Xin, S. Yun, Y. Wang, *Mater. Today Phys.* **2022**, *27*, 100765.
[24] X. Zhang, X. Hou, J. Gao, Z. Wang, X. Zhao, C. Xu, D. Gao, *J. Mater. Chem. C* **2023**, *11*, 16631.
[25] D. Gao, J. Gao, F. Gao, Q. Kuang, Y. Pan, Y. Chen, *Z. Pan, Journal of Materials Chemistry C* **2021**, *9*, 16634.
[26] J. Xing, Y. Zhao, M. Askerka, L. N. Quan, X. Gong, W. Zhao, J. Zhao, H. Tan, G. Long, L. Gao, Z. Yang, O. Voznyy, J. Tang, Z. H. Lu, Q. Xiong, E. H. Sargent, *Nature Commun* **2018**, *9*, 3541.
[27] Y. Wu, X. Li, H. Zeng, *ACS Energy Lett.* **2019**, *4*, 673.
[28] Y. Tong, E. Bladt, M. F. Aygüler, A. Manzi, K. Z. Milowska, V. A. Hintermayr, P. Docampo, S. Bals, A. S. Urban, L. Polavarapu, J. Feldmann, *Angew. Chem., Int. Ed.* **2016**, *55*, 13887.
[29] F. Liu, Y. Zhang, C. Ding, S. Kobayashi, T. Izuishi, N. Nakazawa, T. Toyoda, T. Ohta, S. Hayase, T. Minemoto, K. Yoshino, S. Dai, Q. Shen, *ACS Nano* **2017**, *11*, 10373.
[30] L. Protesescu, S. Yakunin, M. I. Bodnarchuk, F. Krieg, R. Caputo, C. H. Hendon, R. X. Yang, A. Walsh, M. V. Kovalenko, *Nano Lett.* **2015**, *15*, 3692.
[31] B. Zhao, M. Abdi-Jalebi, M. Tabachnyk, H. Glass, V. S. Kamboj, W. Nie, A. J. Pearson, Y. Puttisong, K. C. Gödel, H. E. Beere, D. A. Ritchie, A. D. Mohite, S. E. Dutton, R. H. Friend, A. Sadhanala, *Adv. Mater.* **2017**, *29*, 1604744.
[32] Z. Xiao, L. Zhao, N. L. Tran, Y. L. Lin, S. H. Silver, R. A. Kerner, N. Yao, A. Kahn, G. D. Scholes, B. P. Rand, *Nano Lett.* **2017**, *17*, 6863.
[33] G. E. Eperon, S. D. Stranks, C. Menelaou, M. B. Johnston, L. M. Herz, H. J. Snaith, *Energy Environmental Science* **2014**, *7*, 982.
[34] Q. Zhang, R. Su, W. Du, X. Liu, L. Zhao, S. T. Ha, Q. Xiong, *Small Methods* **2017**, *1*, 1700163.
[35] S. Liu, B. Yang, J. Chen, D. Zheng, Z. Tang, W. Deng, K. Han, *Laser Photonics Rev.* **2022**, *16*, 2100439.
[36] G. E. Eperon, D. S. Ginger, *ACS Energy Lett.* **2017**, *2*, 1190.
[37] B. Luo, F. Li, K. Xu, Y. Guo, Y. Liu, *Z. Xia, J. Z. Zhang, Journal of Materials Chemistry C* **2019**, *7*, 2781.
[38] Y. Zhou, J. Chen, O. M. Bakr, H. T. Sun, *Chem. Mater.* **2018**, *30*, 6589.
[39] J. Hieulle, D. Y. Son, A. Jamshaid, X. Meng, C. Stecker, R. Ohmann, Z. Liu, L. K. Ono, Y. Qi, *Adv. Funct. Mater.* **2023**, *33*, 2211097.
[40] L. Xu, J. Chen, J. Song, J. Li, J. Xue, Y. Dong, B. Cai, Q. Shan, B. Han, H. Zeng, *ACS Applied Materials Interfaces* **2017**, *9*, 26556.
[41] X. Yu, L. Wu, D. Yang, M. Cao, X. Fan, H. Lin, Q. Zhong, Y. Xu, Q. Zhang, *Angew. Chem.* **2020**, *132*, 14635.
[42] J. Chen, Y. Zeng, R. Sun, W. Zhang, Y. Huang, J. Zheng, Y. Chi, *Small* **2023**, *19*, 2301010.
[43] Z. Wang, J. Lai, Q. Huang, D. Wu, F. Qi, N. Zhang, Y. Pu, C. Tian, W. Chen, Y. Liu, P. He, K. An, X. Tang, F. Wang, Y. Liu, G. Han, *Adv. Opt. Mater.* **2023**, *11*, 2300399.
[44] B. A. Rosales, K. Schutt, J. J. Berry, L. M. Wheeler, *ACS Energy Lett.* **2023**, *8*, 1705.
[45] Y. Zhao, K. Zhu, *Chem. Commun.* **2014**, *50*, 1605.
[46] D. B. Straus, S. Guo, R. J. Cava, *J. Am. Chem. Soc.* **2019**, *141*, 11435.
[47] A. M. A. Leguy, Y. Hu, M. Campoy-Quiles, M. I. Alonso, O. J. Weber, P. Azarhoosh, M. van Schilfgaarde, M. T. Weller, T. Bein, J. Nelson, P. Docampo, P. R. F. Barnes, *Chem. Mater.* **2015**, *27*, 3397.
[48] M. I. Dar, G. Jacopin, S. Meloni, A. Mattoni, N. Arora, A. Boziki, S. M. Zakeeruddin, U. Rothlisberger, M. Grätzel, *Sci. Adv.* **2016**, *2*, 1601156.
[49] A. J. Barker, A. Sadhanala, F. Deschler, M. Gandini, S. P. Senanayak, P. M. Pearce, E. Mosconi, A. J. Pearson, Y. Wu, A. R. Srimath Kandada, T. Leijtens, F. De Angelis, S. E. Dutton, A. Petrozza, R. H. Friend, *ACS Energy Lett.* **2017**, *2*, 1416.
[50] S. Masi, A. F. Gualdrón-Reyes, I. Mora-Seró, *ACS Energy Lett.* **2020**, *5*, 1974.
[51] L. M. Wheeler, D. T. Moore, R. Ihly, N. J. Stanton, E. M. Miller, R. C. Tenent, J. L. Blackburn, N. R. Neale, *Nature Commun* **2017**, *8*, 1722.
[52] G. Grancini, M. K. Nazeeruddin, *Nature Review Materials* **2019**, *4*, 4.
[53] J. V. Milić, *J. Mater. Chem. C* **2021**, *9*, 11428.
[54] R. L. Z. Hoye, J. Hidalgo, R. A. Jagt, J. P. Correa-Baena, T. Fix, J. L. MacManus-Driscoll, *Adv. Energy Mater.* **2022**, *12*, 2100499.
[55] M. I. Saidaminov, J. Almutlaq, S. Sarmah, I. Dursun, A. A. Zhumekenov, R. Begum, J. Pan, N. Cho, O. F. Mohammed, O. M. Bakr, *ACS Energy Lett.* **2016**, *1*, 840.
[56] S. K. Sharma, M. Salesh, M. R. Subramaniam, B. Attarwala, A. Yella, *ACS Energy Lett.* **2023**, *8*, 2259.
[57] S. K. Sharma, C. Phadnis, T. K. Das, A. Kumar, B. Kavaipatti, A. Chowdhury, A. Yella, *Chem. Mater.* **2019**, *31*, 3111.
[58] B. A. Rosales, L. E. Mundt, L. T. Schelhas, L. M. Wheeler, *J. Am. Chem. Soc.* **2022**, *144*, 667.
[59] B. A. Rosales, L. E. Mundt, T. G. Allen, D. T. Moore, K. J. Prince, C. A. Wolden, G. Rumbles, L. T. Schelhas, L. M. Wheeler, *Nat. Commun.* **2020**, *11*, 5234.
[60] S. K. Sharma, A. Tiwari, M. Arjumand, A. Yella, *Nanoscale* **2024**, *16*, 11028.
[61] B. A. Rosales, J. Kim, V. M. Wheeler, L. E. Crowe, K. J. Prince, M. Mirzokarimov, T. Daligault, A. Duell, C. A. Wolden, L. T. Schelhas, L. M. Wheeler, *Adv. Energy Mater.* **2023**, *13*, 2203331.
[62] L. Wang, H. Liu, Y. Zhang, O. F. Mohammed, *ACS Energy Lett.* **2020**, *5*, 87.
[63] Y. Zhang, M. I. Saidaminov, I. Dursun, H. Yang, B. Murali, E. Alarousu, E. Yengel, B. A. Alshankiti, O. M. Bakr, O. F. Mohammed, *J. Physical Chemistry Letters* **2017**, *8*, 961.
[64] S. K. Sharma, S. Mamgain, B. Attarwala, A. Yella, *Nanoscale Adv* **2019**, *1*, 2502.
[65] Z. Wang, Y. Zhang, X. Liu, Y. Yu, F. Xu, J. Ding, X. Liang, K. Yang, W. Xiang, *Adv. Mater. Technol.* **2021**, *6*, 2100654.
[66] B. Zhou, M. Han, Y. He, R. Qian, W. Xiong, C. Zhao, L. He, A. Pan, *Cryst. Growth Des.* **2024**, *24*, 301.
[67] H. Zhao, T. Lin, S. Shi, W. Bai, T. Xuan, T. Zhou, R. J. Xie, *J. Mater. Chem. C* **2022**, *10*, 7552.
[68] X. Feng, P. Xu, J. Liu, X. Zhao, J. Cao, J. Liu, *Inorg. Chem.* **2022**, *61*, 17590.
[69] M. C. Brennan, A. Ruth, P. V. Kamat, M. Kuno, *Trechem* **2020**, *2*, 282.
[70] A. J. Knight, L. M. Herz, *Energy Environmental Science* **2020**, *13*, 2024.
[71] Q. A. Akkerman, *Nano Lett.* **2022**, *22*, 8168.